Energy materials

Facile microwave-assisted hydrothermal synthesis of GdVO$_4$ nanospheres: unlocking their potential as electrodes for supercapacitors

Fernando José Soares Barros[1], Klebson Lucas Pereira Cardoso[1], Elson Longo[2], Auro Atsushi Tanaka[1], Marco Aurélio Suller Garcia[1,*], and Ivo Mateus Pinatti[1,*]

[1] *Department of Chemistry, Federal University of Maranhão, Av. dos Portugueses, 1966, São Luís, MA 65080-805, Brazil*

[2] *Department of Chemistry, CDMF-UFSCar, Federal University of São Carlos, Rod. Washington Luiz km 235, São Carlos, SP 13565-905, Brazil*

ABSTRACT

In the face of current energy and environmental challenges, electrochemical storage devices emerge as a promising alternative. Specifically, supercapacitors are highly valued for their exceptional ability to deliver rapid responses and exhibit high-power capabilities. Although rare-earth compounds have received less attention in the electrochemical storage field, the utilization of nanotechnology tools allows for precise manipulation of their shape and size, which opens new possibilities for developing novel configurations with improved properties, presenting previously unexplored applications. Herein, we set a new electrode material consisting of nanospheres of gadolinium vanadate (GdVO$_4$) synthesized by microwave-assisted hydrothermal method, which was a crucial component in preparing nickel foam-based electrodes. The material was thoroughly characterized, revealing interesting properties for energy storage applications. The electrode delivered a high specific capacitance of 1203.75 F g^{-1} at 1 A g^{-1} and good cycling stability after 500 cycles. Then, an asymmetric supercapacitor was performed, reaching 80.63 F g^{-1} at 1 A g^{-1} and 130.2 Wh kg^{-1} of energy density when the power density was 2880.18 W kg^{-1}. Thus, this study highlights the potential of GdVO$_4$ as an electrode material in electrochemical energy storage applications.

Introduction

Electrochemical storage devices can provide a highly effective answer to the growing energy and environmental crisis that society faces today [1–3].

Although domestic energy utilization is high due to the increasing per capita consumption of primary energy resources, the industrial segment accounts for a large proportion of the total produced energy of the world, which prompts assertive energy solutions

---

Handling Editor: Kyle Brinkman.

Address correspondence to E-mail: marco.suller@ufma.br; ivo.pinatti@ufma.br

Ⓐ Springer

for this sector [4–6]. In this scenario, alternative energy sources such as solar, wind, geothermal, and tide energy offer significant advantages, including reduced greenhouse gas emissions, enhanced energy security, and the potential for long-term sustainability [7]. However, fluctuations are inherent to these energy sources due to their intermittent nature, which demands rapid response energy storage solutions [8]. Thus, supercapacitors can leverage the field due to their fast response and high-power abilities, stabilizing the energy supply by enhancing grid stability and maximizing the integration of renewable energy into our energy systems [9, 10].

Although several studies have been conducted on transition metal oxides (such as NiO, Co_3O_4, and MnO_2) as electrodes for supercapacitors due to their high specific capacitance [10, 11], a research segment has been focusing on rare-earth elements. Such compounds tend to offer stable trivalent ions, in which their unpaired 4f electrons typically are not involved in chemical bondings and could represent unique properties for energy storage [12]. Extensive research focuses on rare-earth-based materials, mainly rare-earth oxides, sulfides, hydroxides, and composites. These materials have acquired significant attention in scientific studies due to their unique properties and potential applications in storage systems [13]. Aiming to introduce novel materials or configurations that could potentially incorporate rare-earth elements or their compounds in supercapacitor technology, recent research has been using nanotechnology tools to obtain shape and size control over the materials [14]. Also, their interaction with well-known ions that present storage applications is important, aiming to raise properties not observed before.

Vanadium (V) is an abundant occurring element in the Earth's crust [15]. Its ability to exist in multiple valence states results in various compounds in nature [16], which make vanadium-based materials suitable for utilization as electrode materials in supercapacitors. Among several vanadium-based compounds, vanadates (VO_4^{3-}) can undergo easily reversible redox reactions, which means they can efficiently store and release electrical energy through chemical transformations [17]. Gadolinium (Gd), a member of rare-earth elements, is not commonly used as a material for supercapacitor electrodes itself. However, it finds application as a dopant for transition metal oxides or as a component of composites prepared with electroactive polymers [18–20]. Also, gadolinium vanadate

($GdVO_4$) is not extensively explored to prepare supercapacitor electrodes.

Herein, we proposed an innovative preparation of an electrode for electrochemical storage comprised of well-defined nanospheres of $GdVO_4$ prepared by a microwave-assisted hydrothermal (MAH) method. The material was fully characterized by field emission scanning electron microscopy (FE-SEM), X-ray photoelectron spectroscopy (XPS), Raman, and X-ray diffraction (XRD), giving rise to potential properties that match unprecedented performance in the literature using a Gd-based material. The electrode delivered a high specific capacitance of 1203.75 F g^{-1} at 1 A g^{-1}. An assembled asymmetric supercapacitor was also performed, reaching 80.63 F g^{-1} at 1 A g^{-1} and 130.2 Wh kg^{-1} of energy density when the power density was 2880.18 W kg^{-1}.

Experimental section

Sample preparation

$GdVO_4$ nanospheres were synthesized using Gd_2O_3 (99.99%, Sigma-Aldrich), NH_4VO_3 (99.9%, Sigma-Aldrich), and HNO_3 (65%, Synth) as precursors. The solutions were prepared as follows: Firstly, $Gd(NO_3)_3$ solution was prepared by dissolving Gd_2O_3 in concentrated HNO_3 solution under magnetic stirring at 60 °C. Separately, 1.0 mmol of the $Gd(NO_3)_3$ was added to 45 mL of deionized water at 90 °C under stirring. Similarly, NH_4VO_3 was dissolved in 45 mL of deionized water at 90 °C under stirring. Then, the two precursors' solutions were mixed under constant stirring for 30 min. This procedure promoted the co-precipitation of the amorphous $GdVO_4$ in the reactional mixture. This mixture was transferred to a 100-mL Teflon autoclave, reaching 90% of its total volume, allowing the maximum pressure efficiency. The autoclave was finally sealed and placed in the MAH system using 2.45 GHz microwave radiation with a maximum power of 800 W. The reactional mixture was heated at 160 °C under a nominal heating rate of 140°/min (at 800 W) by direct interaction of water molecules with microwave radiation and remained under a constant pressure of 2.5 bar for 32 min. After that, the autoclave was naturally cooled to room temperature. Finally, the solid product was water washed several times until neutral pH; then, it was dried at 80 °C for 12 h.

Measurements and characterization

The nanocrystals were structurally characterized by X-ray diffraction (XRD) using a D/Max-2000PC Rigaku (Japan) diffractometer with Cu Kα radiation (λ = 1.5406 Å) in the 2θ range from 10° to 80° at a scanning speed of 2°/min in the normal routine. The average crystallite size 'd$_{DS}$' was calculated using the Debye–Scherrer relation [Eq. (1)]:

$$d_{DS} = \frac{0.9\lambda}{\beta \cos \theta} \tag{1}$$

where 'β' is the full width at half maxima (FWHM = 1.518 rad) in radians, '2θ' is the diffraction angle in degrees (24.79°), and 'λ' is the wavelength (1.543 Å) of the X-rays employed.

Micro-Raman spectroscopy was conducted on a Horiba Jobin–Yvon (Japan) spectrometer equipped with a charge-coupled device (CCD) detector and argon-ion laser (Melles Griot, USA) operating at 514.5 nm and a maximum power of 200 mW. X-ray photoelectron spectroscopy (XPS) was performed using a ScientaOmicron ESCA + spectrometer with a high-performance hemispheric analyzer (EA 125) with monochromatic Al Kα ($h\nu$ = 1486.6 eV) radiation as the excitation source. The operating pressure in the ultrahigh vacuum chamber (UHV) was 2×10^{-9} mbar during analysis. The survey and high-resolution XPS spectra used energy steps of 50 and 20 eV, respectively. The morphology and sizes of the nanocrystals were observed on a field emission scanning electron microscope (FE-SEM) model Inspect F50 (FEI Company, Hillsboro, OR) operating at 5 kV.

Electrochemical studies

The electrochemical tests were conducted using an Autolab PGSTAT302N potentiostat (Metrohm, The Netherlands) and the NOVA 2.1.4 software for data analysis. A three-electrode electrochemical cell configuration was employed, consisting of an Ag/AgCl reference electrode, a platinum wire counter electrode, and a working electrode comprising a nickel foam coated with the active material (A = 1.5 cm^2). To prepare the ink for the working electrode, the following procedure was followed: a weight ratio of 8:1:1 for the active material, carbon black, and a solution of PVDF (Poly(vinylidene fluoride), Sigma-Aldrich) in N-methyl-2-pyrrolidone (NMP, Sigma-Aldrich) was measured using a Kern 410 analytical balance.

Subsequently, this mixture was homogenized for 10 min in an agate mortar. Then, 20 µL of the resulting ink was deposited onto the nickel foam. The electrode was then dried for 4 h at 60 °C and pressed onto a nickel rod.

The electrochemical studies were performed in KOH 2.0 M electrolyte solution. Cyclic voltammetry (CV) was tested at various scan rates: 5, 10, 20, 40, and 80 mV s^{-1} at a potential range of 0.2–0.5 V. The galvanostatic charge–discharge (GCD) studies were performed at current densities range from 1 to 15 A g^{-1}. To evaluate the stability of the material, a 3100-cycle test was performed with electrochemical impedance spectroscopy studies (EIS) in a range of 0.1–1000 Hz.

The specific capacitance (F g^{-1}) was calculated from the GCD curves using Eq. (2):

$$Cs = \frac{I \times \Delta t}{\Delta V \times m} \text{F g}^{-1} \tag{2}$$

where C$_s$ is specific capacitance, I is the current, Δt in (s) is the discharge time, ΔV in voltage represents the potential drop, and m is the mass of the electrode material in mg.

To calculate the Coulombic efficiency (η), Eq. (3) was used [21]:

$$\eta = \frac{t_d}{t_c} \times 100 \% \tag{3}$$

where t_d is the discharging time and t_c is the charging time.

The asymmetric cell was performed in a configuration of two electrodes, one working electrode containing the active material and the other with activated carbon. The preparation of both electrodes followed the same procedure mentioned above. First, the electrochemical tests were performed with the carbon electrode in the three electrodes' configuration to obtain its current and specific capacitance values. These values were used with those of the active material to calculate the required amount of activated carbon for the electrode to be used in the asymmetric cell tests, following the mass/charge, according to Eq. (4) [21]:

$$\frac{m+}{m-} = \frac{Q+}{Q-} = \frac{m \times Cs \times \Delta V}{m \times Cs \times \Delta V} \tag{4}$$

where $m+-$ and $Q+-$ mean the mass/charge balance, m is the mass (mg), Cs is specific capacitance, and ΔV in voltage represents the potential drop of activated carbon and the active material.

The energy density (ED) was calculated using Eq. (5) [22]:

$$ED = \frac{1}{2} \cdot C_s (\Delta V)^2 \tag{5}$$

where C_s is the specific capacitance (F g^{-1}) obtained in the GCD tests for the asymmetric supercapacitor and ΔV (V) is the potential range between the cathode and anode.

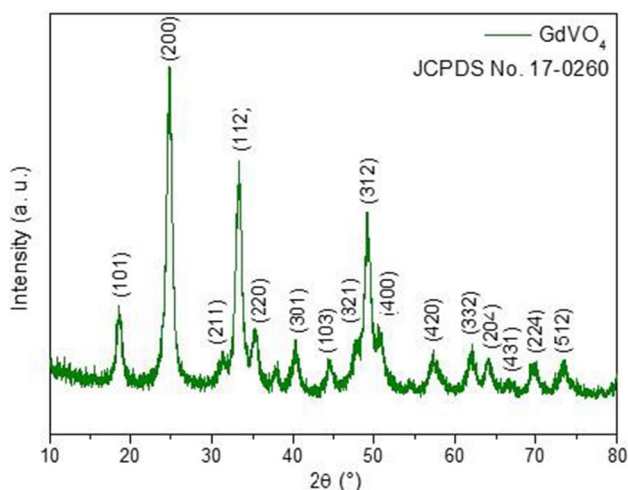The power density (PD) was obtained with Eq. (6) [22]:

$$PD = 3600 \times \frac{ED}{\Delta t} \tag{6}$$

where Δt (s) is the time of discharge of the device. All the tests were carried out at room temperature.

Results and discussion

Structural and morphological characterizations

Figure 1 shows the XRD pattern of the GdVO$_4$ nanospheres. The material presents a tetragonal system with a zircon-type structure and *I41/amd* space group, corresponding to the lanthanide vanadates (LnVO$_4$) structure. The reference pattern of pure GdVO$_4$ (JCPDS card No. 17-0260) was perfectly indexed to the experimental phase obtained, and the characteristic peak broadening observed was caused by the nanometric size of the crystallites [23, 24]. The most intense reflection peak observed at 24.9° corresponds to the

(200) plane in the tetragonal structure. The average crystallite size 'd_{DS}' was estimated to be around 94 nm, similar to the reported ones [24–26].

The structural order in the short range for the GdVO$_4$ nanospheres was determined by Raman spectroscopy. GdVO$_4$ crystallizes in the zircon-type structure with space group *I4$_1$/amd*. According to factor group analysis, there are 12 Raman active modes at the center of the Brillouin zone, as stated by the following irreducible representation: $\Gamma = 2A_{1g} + 4B_{1g} + B_{2g} + 5E_g$. The modes observed in the region 260–1000 cm^{-1} are internal stretching and bending vibrations of the VO$_4$ tetrahedra, and the modes observed at 119, 154, and 231 cm^{-1} are external ones [27]. Figure 2 shows the Raman spectra of the GdVO$_4$ nanospheres excited at 514.5 nm. Intense and defined nine Raman modes are found at 119, 154, 231, 262, 378, 476, 791, 804, and 866 cm^{-1}, which can be assigned to the B_{1g}, E_g, E_g, B_{2g}, A_{1g}, B_{1g}, B_{1g}, E_g, and A_{1g} modes, respectively. They agree with the reported literature and confirm the structural short-range order of the nanospheres [28].

XPS analysis identified the chemical composition, binding energy, and oxidation state of elements on the GdVO$_4$ nanospheres' surface. The binding energies were obtained by calibrating the spectra through the C 1s peak at 285 eV. Figure 3A shows the survey XPS spectra of the sample, and it identified Gd 4d, V 2p, and O 1s orbitals. The C 1s contamination peak observed can be ascribed to adventitious hydrocarbon from the XPS instrument.

A high-resolution XPS spectrum of each element was carried out to analyze the materials further.

**Figure 1** XRD diffraction pattern of GdVO$_4$ nanospheres.
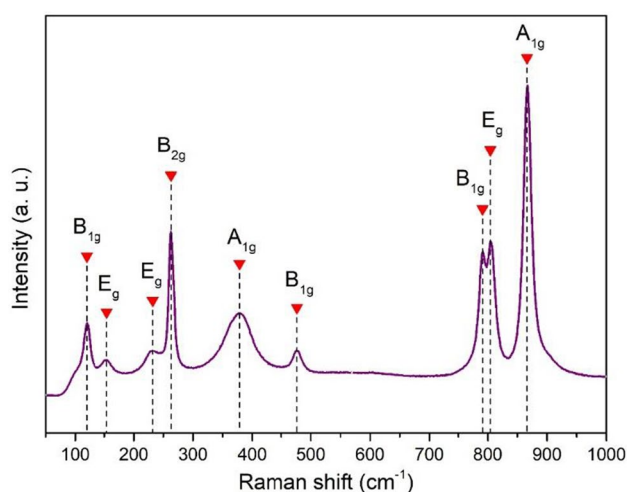
Figure 2 Raman spectra of the GdVO$_4$ nanospheres.
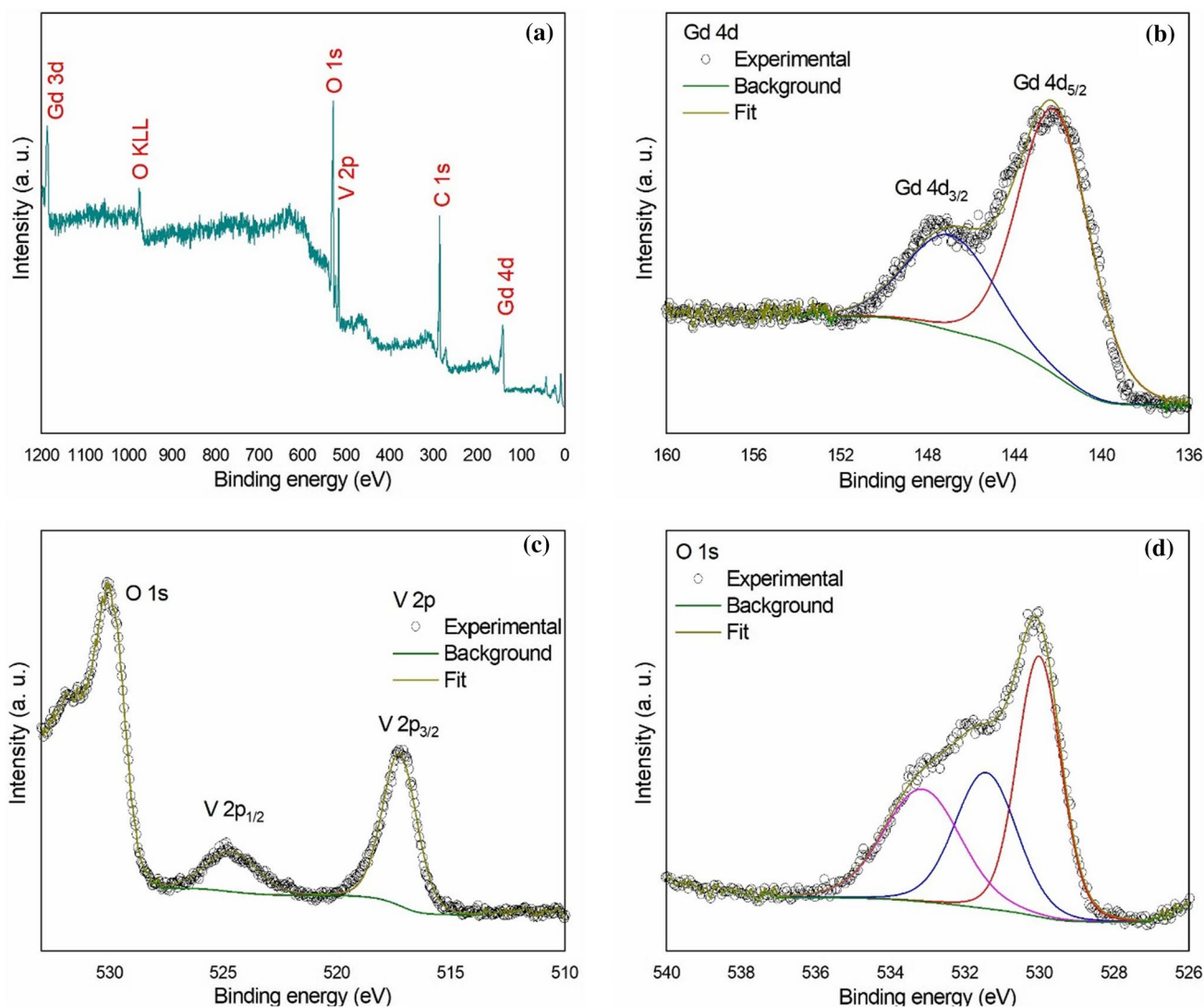
Figure 3 XPS spectra of the GdVO$_4$ nanospheres. **a** survey; **b** Gd 4d; **c** V 2p; and **d** O 1s.

The number of appropriate components was added for each spectrum, and a Shirley-type background was used for the fitting. The Gd 4d high-resolution XPS spectrum is shown in Fig. 3B. The spectrum presents two peaks at binding energy (BE) of 142.1 and 146.9 eV due to Gd 4$d_{5/2}$ and Gd 4$d_{3/2}$ orbitals, which can be ascribed to the Gd^{3+} valence state [29, 30]. The V 2p high-resolution XPS spectrum is shown in Fig. 3c. Except for the vanadium oxides, V metal gives asymmetric peak shapes in the V 2p region. V 2p peak has significantly split spin–orbit components (Δ_{metal}=7.6 eV), and the splitting Δ-value varies with the chemical state (Δ_{V2O5} = 7.4 eV). Also, FWHM for each spin–orbit component is the same, but for V 2p, the V 2$p_{1/2}$ component is much broader than the

V 2$p_{3/2}$ peak; as a result, the V 2$p_{1/2}$ peak is much shorter than expected. The spectrum was fitted with two components at BE of 517.2 and 524.6 eV, corresponding to V 2$p_{3/2}$ and V 2$p_{1/2}$, respectively, which can be attributed to the V^{5+} oxidation state [30]. Also, there is no multiplet splitting upon deconvolution, as V^{+5} does not present any unpaired electrons. Consequently, these results attest that V^{+5} has not decayed, and other species (V^{+4}, V^{+3}, etc.) are absent due to symmetrical peak fit [31]. The O 1s high-resolution XPS spectrum is presented in Fig. 3D, which was deconvoluted into three peaks. The 530 and 531.4 eV peaks correspond to V–O and Gd–O bonds in a tetragonal lattice of GdVO$_4$, respectively. The 533.1 eV peak can be ascribed to hydroxyl groups/

surface-adsorbed oxygen [32–34]. These findings confirmed the successful formation of GdVO$_4$ nanospheres and their surface elucidation.

FE-SEM images of GdVO$_4$ nanospheres are shown in Fig. 4. The images show regular spherical nanoparticles in the 70–100 nm range. Despite the occurrence of some agglomeration resulting from the sample preparation process, it is evident that the particles exhibit distinct and well-defined spherical morphology. This characteristic is advantageous for our applications, as alternative morphologies could compromise the material's performance. Moreover, the nanospheres demonstrate a uniform surface, as anticipated, owing to the favorable influence of the
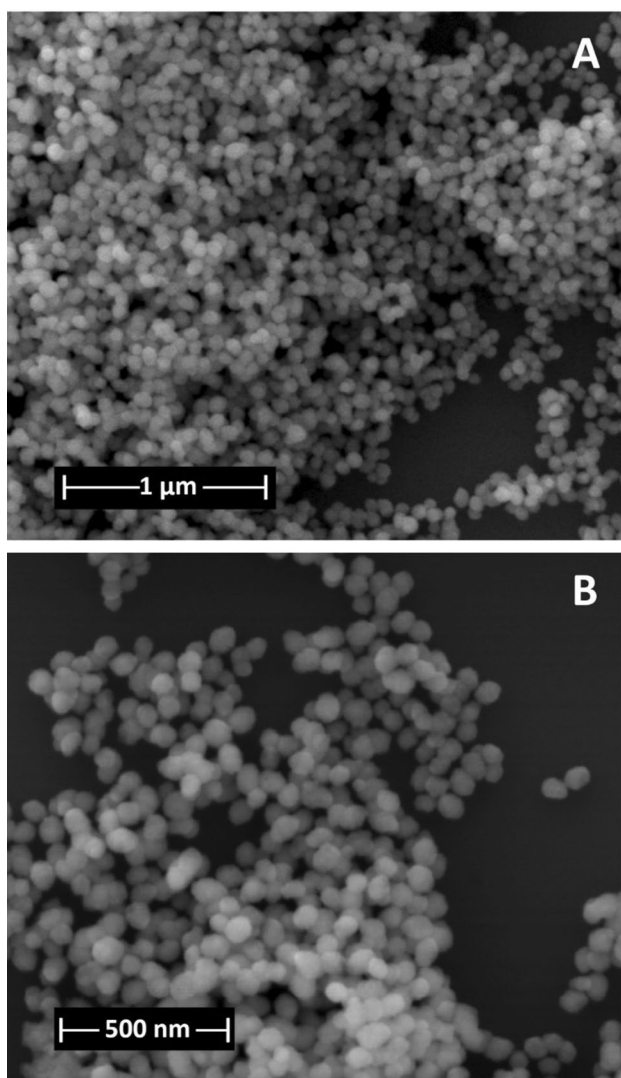

Figure 4 FE-SEM images of the GdVO$_4$ nanospheres with different magnifications: **A** 50 k and **B** 150 k.

pressure and temperature employed in the MAH synthesis procedure, which promotes phase purity.

Electrochemical studies

CV and GCD tests were performed to evaluate the energy storage properties of the prepared GdVO$_4$ nanoperes (Fig. 5). The CV curves at different scan rates (5–80 mVs^{-1}) are shown in Fig. 5A, demonstrating pseudocapacitive characteristics with distinct redox peaks within 0–0.5 V [35]. It is possible to observe the typical shift on the oxidation peaks for higher potentials with the scan rate increase, followed by reduction peaks shifted to lower potentials. Considering the crystal structure of the material elucidated by XRD and the species revealed by XPS, it is believed that the charge transfer reaction occurs at the surface of the material, which could be represented as:

$$GdVO_4 + xK^+ + xe^- \rightarrow K_x(GdVO_4)$$
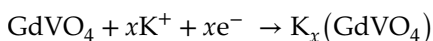
where x is the mole fraction of intercalated K$^+$ ions. It is hypothesized that the presence of VO$_4^{3-}$ components in the crystal contributes more significantly to electron transfer, owing to their high conductivity, possessing the ability to enhance the electrode capacitance substantially. Even though the shape of CV curves is not rectangular at any scan rate, this finding can be ascribed to the electrolyte effect and some possible contributions of the structure shape. In a parallel study, Fend et al. synthesized egg-shaped GdVO$_4$ nanospheres using a 1 M H$_2$SO$_4$ electrolyte. Their research observed no detectable redox reaction, further reinforcing our discussion [28].

The redox peak currents versus the square root of the scan rates were plotted to evaluate the charge transfer behavior, according to Fig. 5B. A well-fitted linear regression with R^2 of 0.9985 and 0.9962 for the anodic and cathodic peaks, respectively, shows a linearity that confirms that the electrodes possess the pseudo-capacitor energy storage mechanism [35, 36]. The GCD tests were performed at current densities range from 1 to 20 A g^{-1} (Fig. 5C). All graphs have a plateau, consistent with the CV curves. The values of specific capacitance, based on the discharge curves and calculated using Eq. (2), were 1203.75 F g^{-1}, 813.33 F g^{-1}, 542.85 F g^{-1}, 314.28 F g^{-1} and 214.28 F g^{-1} at the current density of 1 A g^{-1}, 2 A g^{-1}, 5 A g^{-1}, 10 A g^{-1} and 15 A g^{-1}, respectively. The Coulombic efficiencies were calculated with Eq. (3): 93.15% (1 A g^{-1}), 95.61%
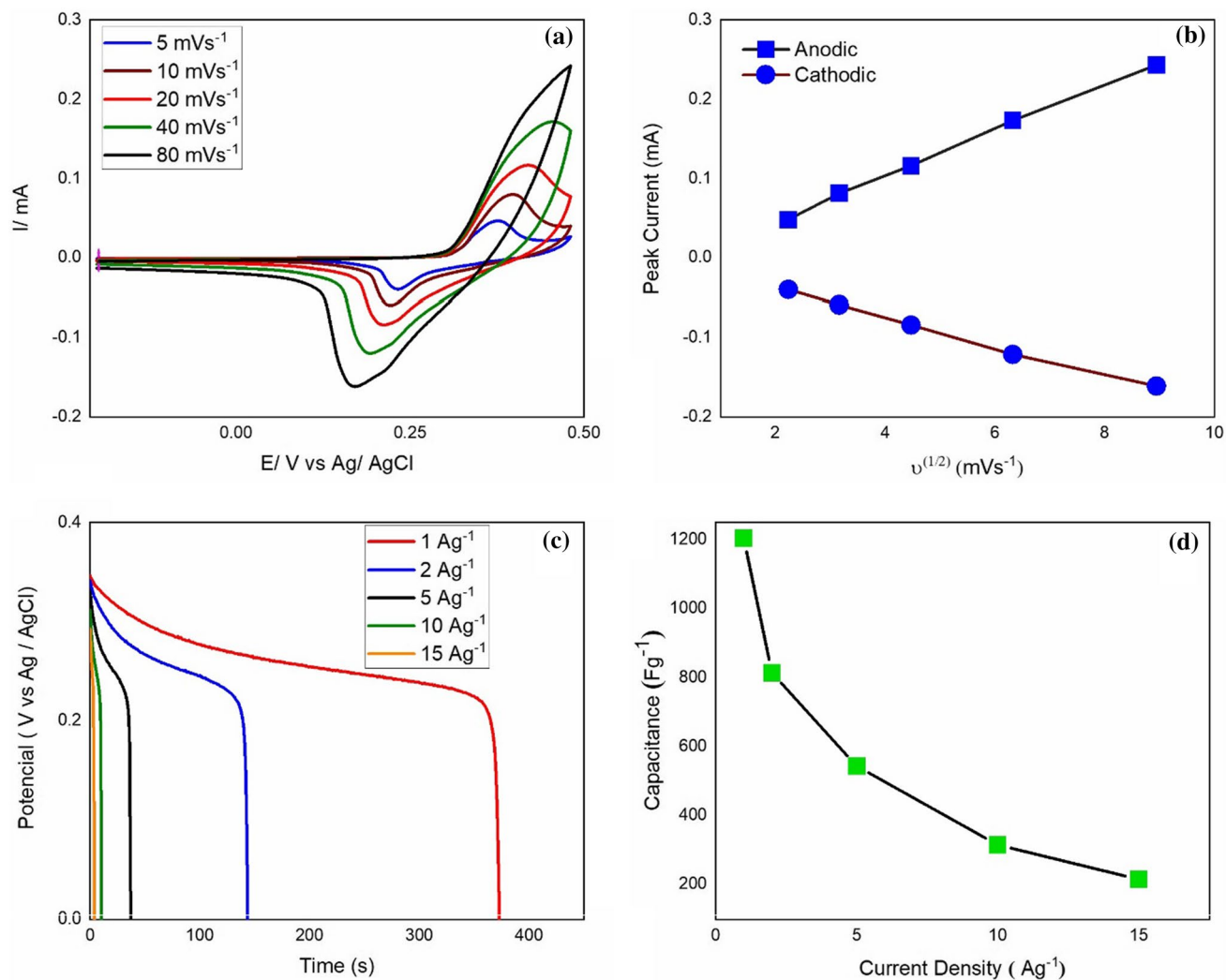
Figure 5 a CV curves for GdVO$_4$ nanospheres at different scan rates; **b** redox peak current versus square root of scan rates; **c** GCD profiles for GdVO$_4$ nanospheres at 1, 2, 5, 10, and 15 A g^{-1}; **d** specific capacitances versus current densities. All the tests were carried out in a 2.0 M KOH solution.

(2 A g^{-1}), 97.44% (5 A g^{-1}), 100% (10 A g^{-1}) and 100% (15 A g^{-1}).

Subsequently, Fig. 5D illustrates the relationship between specific capacitance and current density, allowing for an assessment of the rate capability. As anticipated by prior studies, the specific capacitance values decreased as the current density increased [35, 36]. This observation can be attributed to reduced ion diffusion and decreased ion adsorption on the electrode, particularly at the outer surface of the pores. However, ions have sufficient time to access the electrode's inner and outer surfaces at lower current densities, leading to a higher specific capacitance [21]. The specific capacitance of the GdVO$_4$ nanospheres at

1 A g^{-1} demonstrates excellent performance compared to previous studies, as indicated in Table 1, where it is possible to notice that the morphology and synthesis method influence the supercapacitor performance.

To further investigate the electrochemical performance of the GdVO$_4$ nanospheres for supercapacitors, cycling stability was evaluated by performing 3000 charge–discharge cycles at 20 A g^{-1} (Fig. 6). Figure 6A reveals a progressive increase in its specific capacitance during the initial 1000 cycles, reaching 133 F g^{-1}; this phenomenon can be attributed to the activation of the electrode material.[37] Subsequently, a plateau was attained, succeeded by variations in specific capacitance, which decreased by 20%. Later, in

Table 1 Comparison of specific capacitance (C_s) of GdVO$_4$ nanospheres electrode with previously reported materials

Material	Structure	Synthesis	Electrolyte	C_s (F g^{-1})	Current denstíty (A g^{-1})	References
GdVO$_4$	Nanospheres	Microwave-assisted hydrothermal	2 M KOH	1204	1	This study
Gd$_2$O$_3$/NiS$_2$	Microspheres	Hydrothermal	2 M KOH	354	0.5	[37]
Gd$_2$NiMnO$_6$	Double perovskite	Wet chemical route	4 M KOH	400	1	[35]
Gd^{+3} doped V$_2$O$_5$/MXene	Orthorhombic	Wet chemical route	1.0 M K$_2$SO$_4$	1009	2	[38]
VO$_2$(B)/rGO composite	Nanobelts	Hydrothermal	0.5 M K$_2$SO$_4$	353	1	[39]
VO$_2$–N	Microarray	Organic–inorganic liquid interface	1 M Na$_2$SO4	265	1	[40]

C_s specific capacitance
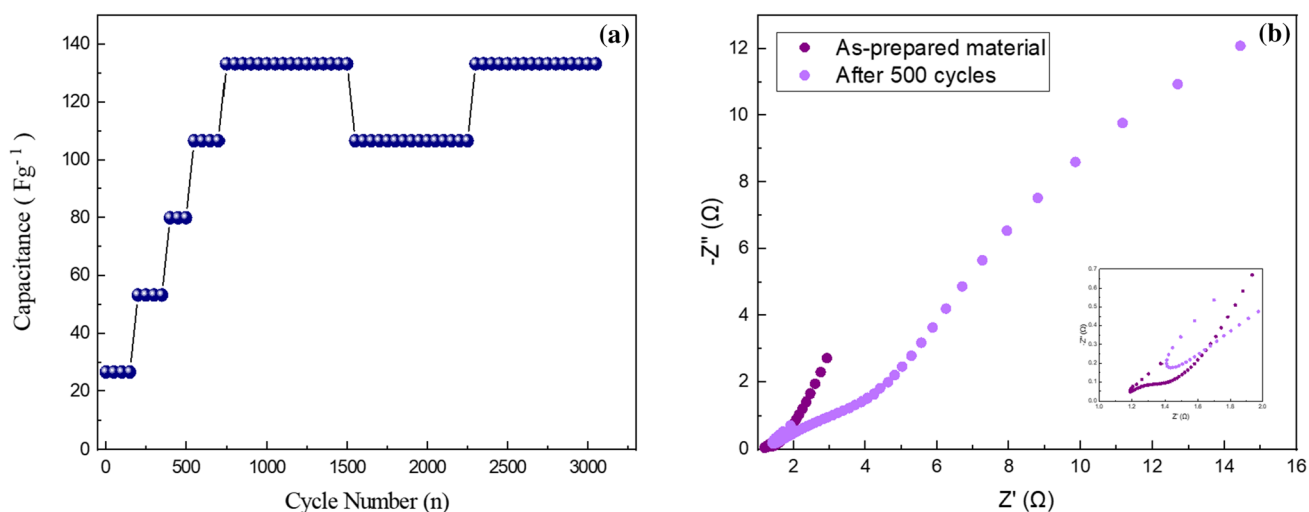
Figure 6 **a** Specific capacitances versus number of cycles at 12 A g^{-1} and **b** EIS analysis in as-prepared material and after 500 charge–discharge cycles of the prepared GdVO$_4$ nanospheres. Tests were performed in 2.0 M KOH solution.

the concluding cycles covering from 2350 to 3100, the system once again achieved a specific capacitance of 133 F g^{-1}.

To assess the resistance of GdVO$_4$ nanospheres during cycling, EIS was conducted on the as-prepared material and after 500 cycles. Figure 6B illustrates the corresponding Nyquist plots, in which a perfect line parallel to the imaginary axis could not be seen, indicating that a constant phase element (CPE) would be needed in the system. Before utilizing the material, we observed that the data tended to have a higher imaginary part, indicating a high capacitive contribution. After the cycling, the slope for this is equivalent to 0.5, suggesting that a mass transport limitation takes place.

To study the practical implementation of GdVO$_4$ nanospheres, an asymmetric supercapacitor cell (ASC) was assembled using it as the anode and activated carbon as the cathode. Upon substituting the values

acquired from the prior GCD analysis into Eq. (4) for the three-electrode system, in conjunction with the outcomes from the activated carbon, a mass balance ratio of 10 was computed, leading to the preparation of the new activated carbon.

The results of the electrochemical tests are presented in Fig. 7. The rectangle-like CV curves (Fig. 7A) indicate the contribution of the pseudocapacitance mechanism for energy storage. An operating voltage window of −0.2 to 1.6 V was obtained. The shape of the CV curves was maintained at high scan rates, showing a high-rate capability [21, 36, 41].

From the ASC (Fig. 7B), the specific capacitances were calculated using Eq. (2): 80.63, 70, 50, 40, 37.5, 37.5, and 25 F g^{-1} at the current densities of 1, 2, 5, 8, 10, 15, 20 A g^{-1}, respectively. Figure 7C shows that the ASC kept rate performance upon increasing the current density, especially from 8 to 15 A g^{-1}. The
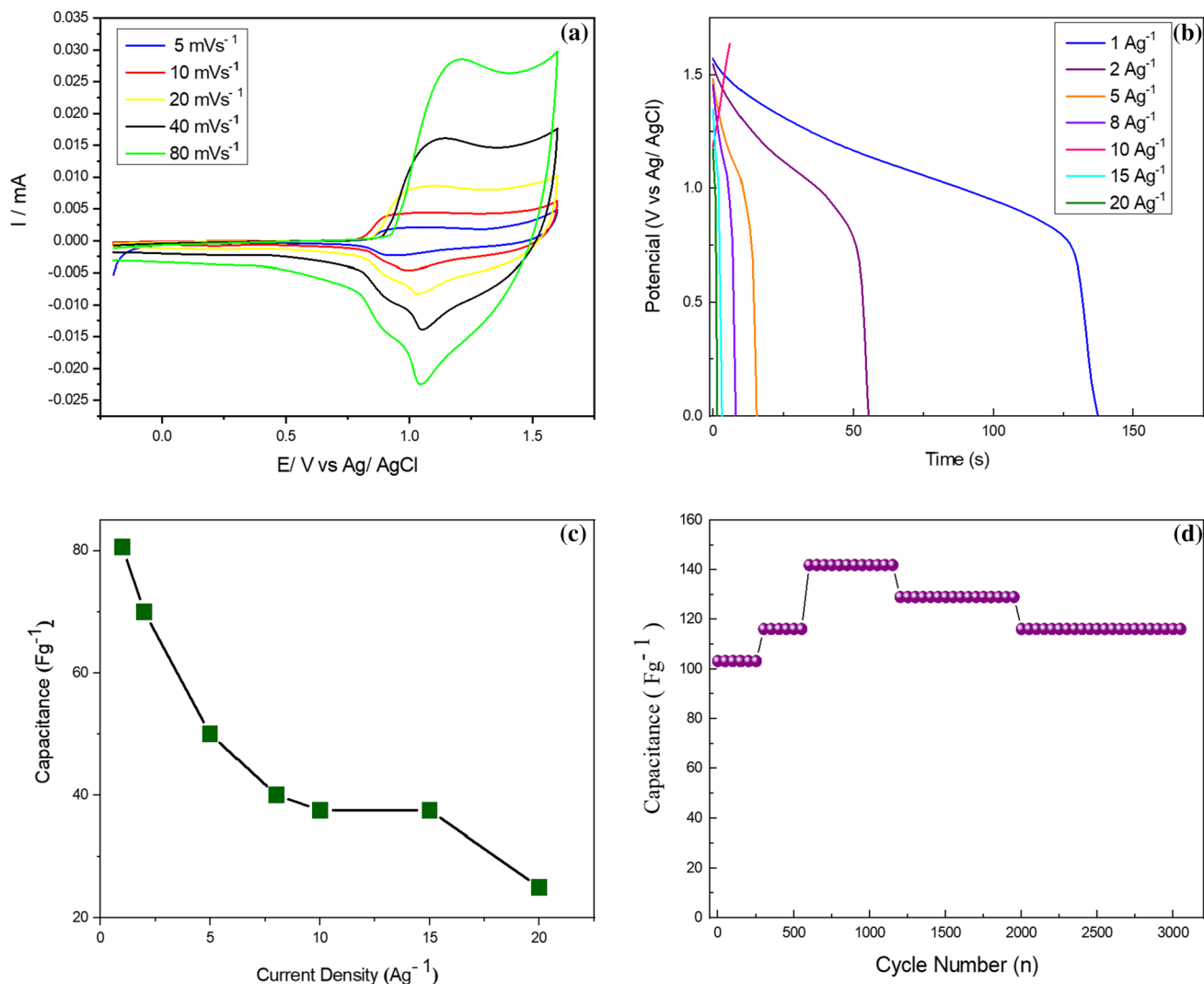
Figure 7 **a** Cyclic voltammetry curves at different scan rates for the hybrid system and **b** charge–discharge profiles at 1, 2, 5, 8, 10, 15, and 20 A g⁻¹. **c** Specific capacitances versus current den-sities. **d** stability after 3000 cycles at 20 A g⁻¹. Tests were performed in 2.0 M KOH solution.

Coulomb efficiencies were 95.56% (1 A g^{-1}), 94.92% (2 A g^{-1}), 97.06 (5 A g^{-1}), 94.44 (8 A g^{-1}), and 100.00% (10.15 and 20 A g^{-1}). The ASC led to a high energy density value of 130.2 Wh kg^{-1} at a power density of 2880.18 W kg^{-1}(at 1 A g^{-1} in 2.0 M KOH). These are outstanding results compared to the current litera-ture, according to Table 2. The GdVO$_4$ nanospheres/ activated carbon was subjected to cycling at 20 A g^{-1} to evaluate its stability (Fig. 7D). Similar to the three-elec-trode system, the specific capacitance of this system experiences an initial increase in the first 1000 cycles, peaking at 142 F g^{-1}. Subsequently, it exhibits two pla-teaus: one at 129 F g^{-1} spanning cycles 1200 to 1950 and another at 116 F g^{-1} between cycles 1951 and 3100.

Conclusions

This study highlights the potential of electrochemi-cal storage electrodes, being a promising solution to address the current energy and environmental challenges. It also introduces a new electrode mate-rial (based on GdVO$_4$ nanospheres) synthesized using a microwave-assisted hydrothermal method, which is vital in preparing nickel foam-based elec-trodes. A thorough characterization of the mate-rial revealed its outstanding properties for energy storage applications. The electrode exhibited a high specific capacitance of 1203.75 F g^{-1} at 1 A g^{-1} and demonstrated good cycling stability after 500

Table 2 Performance of the GdVO$_4$/activated carbon ASC compared with the literature for similar systems

Material	Anode structure	Operating potential (V)	Electrolyte	ED (Wh kg^{-1})	PD (W kg^{-1})	References
GdVO$_4$//activated carbon	Nanospheres	1.6	2 M KOH	130.2	2880.18	This study
V$_2$O$_5$@3DGr//Fe$_3$O$_4$@3DGr	Nanospheres intercalated graphene sheets	1.8	1 M Na$_2$SO$_4$	54.9	898	[21]
GdMnO$_2$/Ni(OH)$_2$//Fe$_3$O$_4$/GO	Nanorod/nanosheets	1.6	2 M KOH	60.25	2332	[36]
V$_2$O$_5$//RGO	Nanobelts	1.7	1 M Na$_2$SO$_4$	50.3	850.9	[41]
VO$_2$//carbonized iron-polyaniline	Nanosheets	1.6	6 M KOH	30	713	[42]

ED energy density, *PD* power density

cycles. Furthermore, an asymmetric supercapacitor constructed using the GdVO$_4$ electrode achieved a specific capacitance of 80.63 F g^{-1} at 1 A g^{-1} and an energy density of 130.2 Wh kg^{-1}, with a power density of 2880.18 W kg^{-1}. These findings highlight the potential of rare-earth-based materials, particularly GdVO$_4$, as a valuable electrode for energy storage applications. Overall, this study contributes to understanding rare-earth-based materials and their potential implications in advancing storage technologies.

Data and code availability

Available under request.

Acknowledgements

Author contributions

FJSB and KLPC contributed to experimental design, carrying out measurements, and manuscript composition. EL and AAT contributed to manuscript composition. MASG and IMP contributed to conception, experimental design, carrying out measurements, and manuscript composition.

Declarations

Conflict of interest   There are no conflicts to declare.

Ethical approval   Not applicable.

References

[1] Wang L, Hu X (2018) Recent advances in porous carbon materials for electrochemical energy storage. Chem Asian J 13:1518–1529. https://doi.org/10.1002/asia.201800553

[2] Kim BK, Sy S, Yu A, Zhang J (2015) Electrochemical supercapacitors for energy storage and conversion. In: Yan J (ed) Handbook of clean energy systems. Wiley Ltd, Chichester, pp 1–25. https://doi.org/10.1002/9781118991978.hces112

[3] Díaz-Ramírez M, Ferreira V, García-Armingol T, López-Sabirón A, Ferreira G (2020) Environmental assessment of electrochemical energy storage device manufacturing to

identify drivers for attaining goals of sustainable materials 4.0. Sustainability 12:342–362. https://doi.org/10.3390/su12010342

[4] Liu Z (2015) Global energy development: the reality and challenges. Glob Energy Interconnect. https://doi.org/10.1016/B978-0-12-804405-6.00001-4

[5] Wang H, Zhang J, Fang H (2017) Electricity footprint of China's industrial sectors and its socioeconomic drivers. Resour Conserv Recycl 124:98–106. https://doi.org/10.1016/j.resconrec.2017.04.011

[6] de Lyrio Oliveira L, de Oliveira Ribeiro C, Qadrdan M (2022) Analysis of electricity supply and demand intra-annual dynamics in Brazil: a multi-period and multi-regional generation expansion planning model. Int J Electric Power Energy Syst 137:107. https://doi.org/10.1016/j.ijepes.2021.107886

[7] Abe JO, Popoola API, Ajenifuja E, Popoola OM (2019) Hydrogen energy, economy and storage: review and recommendation. Int J Hydrogen Energy 44:15072–15086. https://doi.org/10.1016/j.ijhydene.2019.04.068

[8] Engeland K, Borga M, Creutin J-D, François B, Ramos M-H, Vidal J-P (2017) Space-time variability of climate variables and intermittent renewable electricity production–a review. Renew Sustain Energy Rev 79:600–617. https://doi.org/10.1016/j.rser.2017.05.046

[9] Worku MY (2022) Recent advances in energy storage systems for renewable source grid integration: a comprehensive review. Sustainability 14:5985. https://doi.org/10.3390/su14105985

[10] Teixeira LT, de Lima SLS, Rosado TF, Liu L, Vitorino HA, dos Santos CC, Mendonça JP, Garcia MAS, Siqueira RNC, da Silva AGM (2023) Sustainable cellulose nanofibers-mediated synthesis of uniform spinel Zn-ferrites nanocorals for high performances in supercapacitors. Int J Mol Sci 24:9169-9187. https://doi.org/10.3390/ijms24119169

[11] Lichchhavi, Kanwade A, Shirage PM (2022) A review on synergy of transition metal oxide nanostructured materials: effective and coherent choice for supercapacitor electrodes. J Energy Storage 55:105692-105716. https://doi.org/10.1016/j.est.2022.105692

[12] Gao W, Wen D, Ho JC, Qu Y (2019) Incorporation of rare earth elements with transition metal–based materials for electrocatalysis: a review for recent progress. Mater Today Chem 12:266–281. https://doi.org/10.1016/j.mtchem.2019.02.002

[13] Zhao H, Xia J, Yin D, Luo M, Yan C, Du Y (2019) Rare earth incorporated electrode materials for advanced energy storage. Coord Chem Rev 390:32–49. https://doi.org/10.1016/j.ccr.2019.03.011

[14] He Y, Zhou W, Xu J (2022) Rare earth-based nanomaterials for supercapacitors: preparation, structure engineering and application. Chemsuschem. https://doi.org/10.1002/cssc.202200469

[15] Pantapasis K, Grumezescu AM (2017) Gold nanoparticles: advances in water purification approaches. In: Grumezescu AM (ed) Water purification. Elsevier, Amsterdam, pp 447–477. https://doi.org/10.1016/B978-0-12-804300-4.00013-7

[16] Taroni A (2017) V for vanadium. Nat Chem 9:602–602. https://doi.org/10.1038/nchem.2787

[17] Yao G, Zhang N, Zhang Y, Zhou T (2021) Nanostructured transition metal vanadates as electrodes for pseudo-supercapacitors: a review. J Nanopart Res 23:57. https://doi.org/10.1007/s11051-021-05158-9

[18] Shiri HM, Ehsani A (2016) Pulse electrosynthesis of novel wormlike gadolinium oxide nanostructure and its nanocomposite with conjugated electroactive polymer as a hybrid and high efficient electrode material for energy storage device. J Colloid Interface Sci 484:70–76. https://doi.org/10.1016/j.jcis.2016.08.075

[19] Adimule V, Yallur BC, Challa M, Joshi RS (2021) Synthesis of hierarchical structured Gd doped α-Sb_2O_4 as an advanced nanomaterial for high performance energy storage devices. Heliyon 7:e08541. https://doi.org/10.1016/j.heliyon.2021.e08541

[20] Poudel MB, Kim HJ (2022) Synthesis of high-performance nickel hydroxide nanosheets/gadolinium doped-α-MnO_2 composite nanorods as cathode and Fe_3O_4/GO nanospheres as anode for an all-solid-state asymmetric supercapacitor. J Energy Chem 64:475–484. https://doi.org/10.1016/j.jechem.2021.05.002

[21] Ghaly HA, El-Deen AG, Souaya ER, Allam NK (2019) Asymmetric supercapacitors based on 3D graphene-wrapped V_2O_5 nanospheres and Fe_3O_4@3D graphene electrodes with high power and energy densities. Electrochim Acta 310:58–69. https://doi.org/10.1016/j.electacta.2019.04.071

[22] Li J, Xiong D, Wang L, Hirbod MKS, Li X (2019) High-performance self-assembly $MnCo_2O_4$ nanosheets for asymmetric supercapacitors. J Energy Chem 37:66–72. https://doi.org/10.1016/j.jechem.2018.11.015

[23] He Y, Cai J, Li T, Wu Y, Lin H, Zhao L, Luo M (2013) Efficient degradation of RhB over $GdVO_4$/g–C_3N_4 composites under visible-light irradiation. Chem Eng J 215–216:721–730. https://doi.org/10.1016/j.cej.2012.11.074

[24] Shu Z, Li MQ, Gan L, Wan L, Chen X, Zhang X, Gui W (2022) A strategy to synthesize highly luminescent $GdVO_4$:Eu3+/CDs nanocomposite based on hydrothermal deposition method and its application in anti-counterfeiting.

J Alloys Compd. https://doi.org/10.1016/j.jallcom.2022.165881

[25] Thirumalai K, Shanthi M, Swaminathan M (2017) Natural sunlight active GdVO$_4$–ZnO nanomaterials for photo–electro-catalytic and self–cleaning applications. J Water Process Eng 17:149–160. https://doi.org/10.1016/j.jwpe.2017.04.001

[26] Mazierski P, Sowik J, Miodyńska M, Trykowski G, Mikołajczyk A, Klimczuk T, Lisowski W, Nadolna J, Zaleska-Medynska A (2019) Shape-controllable synthesis of GdVO$_4$ photocatalysts and their tunable properties in photocatalytic hydrogen generation. Dalton Trans 48:1662–1671. https://doi.org/10.1039/c8dt04225j

[27] Zhang CC, Zhang ZM, Dai RC, Wang ZP, Zhang JW, Ding ZJ (2010) High-pressure Raman and luminescence study on the phase transition of GdVO$_4$:Eu^{3+} microcrystals. J Phys Chem C 114:18279–18282. https://doi.org/10.1021/jp106063c

[28] He A, Feng L, Liu L, Peng J, Chen Y, Li X, Lu W, Liu J (2020) Design of novel egg-shaped GdVO$_4$ photocatalyst: a unique platform for the photocatalyst and supercapacitors applications. J Mater Sci Mater Electron 31:13131–13140. https://doi.org/10.1007/s10854-020-03864-z

[29] Li M, Wang Y, Zheng Y, Fu G, Sun D, Li Y, Tang Y, Ma T (2020) Gadolinium-induced valence structure engineering for enhanced oxygen electrocatalysis. Adv Energy Mater. https://doi.org/10.1002/aenm.201903833

[30] Zhang X, Wang C, Yu C, Teng B, He Y, Zhao L, Fan M (2018) Application of Ag/AgBr/GdVO$_4$ composite photocatalyst in wastewater treatment. J Environ Sci (China) 63:68–75. https://doi.org/10.1016/j.jes.2017.06.020

[31] Ansari A, Mohanta D (2022) Structural and XPS studies of polyhedral europium doped gadolinium orthovanadate (Eu^{3+}:GdVO$_4$) nanocatalyst for augmented photodegradation against congo-red. Phys E Low Dimens Syst Nanostruct. https://doi.org/10.1016/j.physe.2022.115357

[32] Bae JS, Park SS, Hong TE, Kim JP, Yoon JH, Jeong ED, Won MS, Jeong JH (2009) Optical and surface analysis of lithium incorporated GdVO$_4$:Eu^{3+} phosphor powders. Curr Appl Phys. https://doi.org/10.1016/j.cap.2009.01.025

[33] Shandilya P, Mittal D, Sudhaik A, Soni M, Raizada P, Saini AK, Singh P (2019) GdVO$_4$ modified fluorine doped graphene nanosheets as dispersed photocatalyst for mitigation of phenolic compounds in aqueous environment and bacterial disinfection. Sep Purif Technol 210:804–816. https://doi.org/10.1016/j.seppur.2018.08.077

[34] Pinatti IM, Tello ACM, Pereira PFS, Trench AB, Teodoro MD, Rosa ILV, da Silva ABF, Longo E, Andrés J, Simões AZ (2022) Towards a relationship between photoluminescence emissions and photocatalytic activity of Ag$_2$SeO$_4$: combining experimental data and theoretical insights. Dalton Trans 51:11346–11362. https://doi.org/10.1039/d2dt01057g

[35] Kumar A, Kumar A, Kumar A (2020) Energy storage properties of double perovskites Gd$_2$NiMnO$_6$ for electrochemical super-capacitor application. Solid State Sci 105:106252. https://doi.org/10.1016/j.solidstatesciences.2020.106252

[36] Poudel MB, Kim HJ (2021) Synthesis of high-performance nickel hydroxide nanosheets/gadolinium doped-α-MnO$_2$ composite nanorods as cathode and Fe$_3$O$_4$/GO nanospheres as anode for an all-solid-state asymmetric supercapacitor. J Energy Chem 64:475–484. https://doi.org/10.1016/j.jechem.2021.05.002

[37] Dhanalakshmi S, Mathi Vathani A, Muthuraj V, Prithivikumaran N, Karuthapandian S (2020) Mesoporous Gd$_2$O$_3$/NiS$_2$ microspheres: a novel electrode for energy storage applications. J Mater Sci Mater Electron 31:3119–3129. https://doi.org/10.1007/s10854-020-02858-1

[38] Tahir T, Alhashmialameer D, Zulfiqar S, Atia AME, Warsi MF, Chaudhary K, El Refay HM (2022) Wet chemical synthesis of Gd^{+3} doped vanadium oxide/MXene based mesoporous hierarchical architectures as advanced supercapacitor material. Ceram Int 48:24840–24849. https://doi.org/10.1016/j.ceramint.2022.05.135

[39] Lv W, Yang C, Meng G, Zhao R, Han A, Wang R, Liu J (2019) VO$_2$(B) nanobelts/reduced graphene oxide composites for high-performance flexible all-solid-state supercapacitors. Sci Rep 9:1–8. https://doi.org/10.1038/s41598-019-47266-6

[40] Fan Y, Ouyang D, Li BW, Dang F, Ren Z (2018) Two-dimensional VO$_2$ mesoporous microarrays for high-performance supercapacitor. Nanoscale Res Lett 13:1–8. https://doi.org/10.1186/s11671-018-2557-7

[41] Chen Y, Lian P, Feng J, Liu Y, Wang L, Liu J, Shi X (2022) Tailoring defective vanadium pentoxide/reduced graphene oxide electrodes for all-vanadium-oxide asymmetric supercapacitors. Chem Eng J 429:132274. https://doi.org/10.1016/j.cej.2021.132274

[42] Ndiaye NM, Madito MJ, Ngom BD, Masikhwa TM, Mirghni AA, Manyala N (2019) High-performance asymmetric super-capacitor based on vanadium dioxide and carbonized iron-polyaniline electrodes. AIP Adv. https://doi.org/10.1063/1.5091799